Optimization of hydrogen recirculation ejector for proton-exchange membrane fuel cells (PEMFC) systems considering non-equilibrium condensation

Hongbing Ding [a], Panpan Zhang [a], Yuanyuan Dong [a], Yan Yang [b,*]

[a] *Tianjin Key Laboratory of Process Measurement and Control, School of Electrical and Information Engineering, Tianjin University, Tianjin, 300072, China*
[b] *Faculty of Environment, Science and Economy, University of Exeter, Exeter, EX4 4QF, UK*

ABSTRACT

In proton exchange membrane fuel cell (PEMFC) systems, unconsumed hydrogen recirculation is enabled by utilizing an ejector, and the PEMFC system's efficiency is thereby enhanced. Apart from the structural parameters, an ejector's performance is also significantly affected by the non-equilibrium condensation phenomenon. Therefore, the ejector structural parameters' impact upon non-equilibrium condensation intensity and ejector efficiency is investigated under design conditions. Structural optimization of the ejector is performed within its operating range to uphold optimal efficiency in the presence of fluctuations in secondary flow pressure. The result shows that non-equilibrium condensation negatively affects the ejector's efficiency, but its impact diminishes with larger mixing chamber diameters and nozzle divergence angles. The optimized ejector performs best with a 2.40 mm diameter mixing chamber and an 11.0° nozzle divergence angle. On average, the optimized ejector's performance improves by 16.8%, reaching a maximum improvement of 22.8% within the effective operating range.

Nomenclature

Term	
D_m	Diameter of constant-area mixing chamber, m
L_m	Length of constant-area mixing chamber, m
L_{pm}	Length of constant-pressure chamber, m
θ_d	Diffuser angle, °
L_d	Diffuser length, m
θ_h	Convergence angle of nozzle, °
θ	Divergent angle of nozzle, °
L_h	Length of nozzle divergence section, m
D_n	Diameter of nozzle throat, m
Φ^{in}	Inlet relative humidity, %
m_s	Secondary mass flow rate, kg/s
m_p	Primary mass flow rate, kg/s
$P_{s,in}$	Secondary inlet pressure, Pa
$P_{p,in}$	Primary inlet pressure, Pa
P_{out}	Outlet pressure, Pa

1. Introduction

Currently, the escalation in energy consumption and the intensification of global warming trends have far surpassed the capacity of ecosystems to endure, significantly constraining societal and economic development [1]. Hence, the advancement and application of sustainable energy have become of paramount importance [2]. The proton exchange membrane fuel cell (PEMFC) is regarded as one of the energy-saving devices with promising application prospects [3]. They are envisioned to make significant contributions to the sustainable development of energy resources [4]. In typical scenarios, an excess of hydrogen is utilized in the PEMFC anode to alleviate the possibility of fuel deficits. However, liberating unutilized hydrogen directly into the environment not only reduces the efficiency of PEMFC systems but also poses potential environmental harm [5]. Hence, it is essential to recycle surplus hydrogen [6].

PEMFC hydrogen supply systems can be categorized into three types based on hydrogen circulation methods: Flow-Through Anode (FTA) mode, Dead-End Anode (DEA) mode, and Recirculation mode [7]. In the FTA mode, hydrogen continuously flows through the anode, with excess hydrogen directly discharged from the stack, preventing circulation. This method effectively prevents water accumulation and avoids flooding, ensuring good performance and uniform current density.

However, this mode results in lower hydrogen utilization efficiency and poses significant safety risks due to the direct release of unused hydrogen [8]. Therefore, it is rarely used in practice.

In the DEA mode, the anode outlet of the fuel cell is fully sealed, enabling the complete utilization of hydrogen fuel. However, water produced by the reaction continuously accumulates in the anode due to diffusion, leading to inevitable performance decline over time [9]. To address this issue, a purge valve is commonly used to periodically remove accumulated water [10]. Wang et al. [11] developed and tested an ejector for a 10 kW PEMFC system, finding good voltage consistency in DEA mode at low stack current. However, performance deteriorated at high current due to water accumulation in the anode channels. Jian et al. [12] studied a PEMFC with a dead-end anode experimentally. They identified the optimal purge interval and duration for stable voltage and high hydrogen utilization as 14.86 s and 0.44 s, respectively. Nikiforow et al. [13] investigated hydrogen purging across various humidity levels, purge times, and trigger criteria. Their results showed that an optimized exhaust strategy can easily achieve high fuel efficiency (>99%). Wang et al. [14] used a quasi-2D transient model to optimize purge strategies under anode recirculation, finding that a 3% bleed rate is optimal for energy efficiency. Higher bleed rates above 5% reduce the benefits of increased voltage and lower nitrogen content. Tsai et al. [15] developed a mathematical model to study the impact of purge strategies on energy efficiency. They determined that the optimal purge duration is 0.2–0.4 s for a 0.1 V voltage drop and 0.1 s for a 0.1 M fraction of nitrogen. Chen et al. [16] observed severe carbon corrosion in the membrane electrode assembly under the dead-end anode mode. Introducing a time-controlled purge strategy significantly reduced the rate of carbon corrosion. The anode purge strategy by Liu et al. [17] can improve hydrogen utilization efficiency in practical PEMFC systems to 99%, accounting for hydrogen crossover losses.

The recirculation mode uses excess hydrogen to remove water from the stack, separates the liquid water with a gas-liquid separator, and recirculates the hydrogen back to the anode. This mode enhances hydrogen utilization and humidifies the primary flow, maintaining optimal membrane hydration and performance. Despite its structural complexity and control challenges, the recirculation mode achieves a balance of higher efficiency, more uniform current density, and slower performance degradation. Additionally, this mode improves water management. The recirculation process creates forced convection in the anode channels, promptly removing liquid water and preventing deposition and blockage. Hwang [18] analyzed the three modes and found that for stack power below 1.2 kW, the dead-end and recirculation modes have similar efficiencies. However, above 1.2 kW, the recirculation mode has higher system and stack efficiencies. Liu et al. [19] experimentally studied the dynamic characteristics of gas purging in PEMFCs and found that the performance of the fuel cell in the dual-ejector recirculation mode is superior to that in the dead-end mode. Liang et al. [20] studied large-scale PEMFCs under various anode strategies in typical automotive conditions. They found that the recirculation mode's self-humidification effect increased system efficiency to 35.23% under low relative humidity, significantly higher than the 26.51% in the flow-through mode and 29.92% in the DEA mode. Liu et al. [21] used 3D printing to design hydrogen and oxygen recirculation ejectors, finding that the dual-ejector recirculation mode improved PEMFC stack performance by 4.75% compared to the DEA mode at 130 kPa.

The core of the hydrogen recirculation mode is the recirculation component, which currently includes two main types: hydrogen circulation pumps and ejectors. Table 1 summarizes the commonly used recirculation components along with their advantages and disadvantages. Active recirculation systems use hydrogen circulation pumps like roots, claw, vortex, and centrifugal pumps. These pumps adjust speed to control flow rate and pressure, meeting recirculation needs under varying conditions. Circulation pumps offer advantages such as ease of control and a wide operating range. However, they consume electrical

Table 1
Comparison of different hydrogen recirculation components.

hydrogen recirculation components	Advantages	Disadvantages
Roots pumps [23–25]	high operating reliability; low driving power; low cost.	high sealing performance requirements; oil pollution and noise.
Claw pumps [26]	high reliability; compact structure good compression ratio; long service life; strong adaptability to working conditions	need better design of the claw pump tooth profile; poor sealing performance; noise and vibration
Vortex pumps [27]	simple structure; high operating stability	low efficiency; difficulties in machining and assembly.
Centrifugal pumps [51]	high flow rate; simple structure; small size; high efficiency; low cost.	prone to surge
Ejectors [32–38]	compact structure; reliable operation; no moving parts; no pollution; no parasitic power.	sensitive to changes in working conditions; fuel supply and fuel consumption rates need to be matched

energy, increasing parasitic power consumption and reducing PEMFC efficiency. High-speed rotating components also introduce vibration and noise [22]. Gao et al. [7] reviewed hydrogen circulation pumps, detailing mechanical pumps and solutions for safety, vibration, and noise. Kong et al. [23] proposed a backflow groove to reduce outlet pulsation in roots pumps, stabilizing pressure and mass flow, and enhancing fuel cell stack longevity and stability. Feng et al. [24] created a 3D model of the roots pump to predict flow rates and power consumption under different conditions. They derived a relationship between volumetric and isentropic efficiencies from CFD simulations. Xing et al. [25] designed and tested a three-lobe helical rotor roots pump, showing that pressure differential significantly affects flow rate and volumetric efficiency, with leakage being the key efficiency factor. Liang et al. [26] reviewed hydrogen recirculation devices for PEM fuel cells, noting issues with traditional motor-driven compressors, such as high power consumption, leakage, and noise. Han et al. [27] reviewed hydrogen recirculation components for fuel cell vehicles, highlighting the strict design requirements for mechanical pumps and the significant challenges posed by the oil-free design for bearings and seals.

Passive recirculation systems use ejectors to recirculate hydrogen, leveraging the potential energy of fresh hydrogen for passive anode tail gas recirculation [28]. The pressure differential between the hydrogen reservoir and the PEMFC can provide a consistent pressure gradient for the ejector [29]. Primary flow undergoes expansion within the nozzle, resulting in reduced pressure and increased velocity. This lower pressure triggers the secondary flow to enter the mixing chamber. After the blending of primary and secondary flows, the diffuser restores pressure before supplying the fuel cell, completing the recycling of hydrogen gas. Compared to active systems, ejector-based passive recirculation offers high reliability, zero parasitic power consumption, and low maintenance costs [30]. However, it has a narrow operating range and is sensitive to changes in operating conditions [31]. Since the geometric shape is one of the key factors influencing the ejector's efficiency, it should be noted that significant challenges in terms of safety concerns associated with hydrogen, high testing costs for fuel cell stacks, and the complex operational characteristics of fuel cell systems pose considerable challenges to the research of ejectors. Thus, the studies rely on CFD simulations.

Pei et al. [32] developed a hydrogen recirculation ejector Computational Fluid Dynamics (CFD) model equipped with steady-state characteristic equations, subsequently, its primary geometric parameters are optimized. Dong et al. [33] conducted numerical simulations on a steam ejector, confirming that critical back pressure and E_R first increase and then decrease as the mixing chamber length increases. Wang et al. [34] discovered that the optimal CAMC's diameter (Condensing and Mixing

Chamber) varies with operational conditions. Bian et al. [35] evaluated the boundary layer separation effects' impact, with a primary focus on optimizing the structural design based on their evaluation. Liu et al. [36] developed an advanced ejector model and then investigated the effects of pressure variations, changes in water vapor and nitrogen mass fractions, and ejector geometry dimensions. Yin et al. [37] established an innovative model that considers non-axisymmetric flow and then investigates the secondary flow tube's impart of the convergence angle and entrance area. Yang et al. [38] employed a weakly correlated model for the anode pressure drop characteristics, utilizing the porous jump boundary, and investigating the impact of pressure and other parameters. Song et al. [39] assessed a confocal twin-nozzle ejector under various operating conditions and optimized its geometric parameters accordingly. The results indicated that the optimal dimensions for the mixing chamber are 22.0 mm in length and 5.5 mm in diameter. Under standard operating conditions, the efficiency improved by 14.10%. Han et al. [40] assessed the influence of bypass inlet axial angle, position, and position, then determined the optimal result to be 10°, 1.1, and 2 mm, respectively. The entrainment ratio was maximally enhanced by 22.1%. Yu et al. [41] designed a new auxiliary ejector and conducted simulation verification. The working range is significantly influenced by the auxiliary port's position, width, and angle, and the optimal parameters vary with different PEMFC operating powers.

Given the intricate flows within the ejector, the impact of non-equilibrium condensation is considerable and cannot be overlooked. Yang et al. [42] investigated the complex characteristics of steam condensation. The study unveiled an 11.71% overestimation of E_R by the dry gas in comparison to the wet gas. Zhang et al. [43] proposed an improved performance evaluation model for steam ejector to facilitate optimization. The results indicated that the enhanced model demonstrated higher predictive accuracy compared to previous models. Han et al. [44] analyzed the phase change characteristics' impact. The results revealed that condensation is harmful. Li et al. [45] simulated the flow characteristics of the ejector under various operating conditions and structures. The study revealed the impact of double-choking flow characteristics on the ejector as well as the shock waves. Ding et al. [46] developed a novel model considering phase change and entropy transport. The study analyzed phase change characteristics under dry and wet gas models. The results indicated that the model exhibited good predictive capabilities. Li et al. [47] investigated the influence of fluctuating motive pressure. The study provided a mechanistic perspective, revealing the inherent correlation between ejector efficiency and shock waves. Yu et al. [48] investigated the transient properties of turbulent vortices and uncovered the interconnections among operational parameters, fluid flow evolution traits, and structural features of coaxial-nozzle ejectors (CNEs). The findings demonstrate that the maximum enhancement of E_R reaches 17.48%. Han et al. [49] explored condensation and droplet behavior in the ejector. The results indicate that the key factors influencing droplet size is supercooling degree. Under operating conditions, the average droplet phase at the ejector outlet increased by 26.5% relative to the original dimensions. Ding et al. [50] analyzed the exergy performance of the ejector and found that increasing the secondary flow temperature from 60 °C to 80 °C raises exergy destruction from 330.28 kJ/kg to 390.23 kJ/kg, while the destruction rate decreases from 29.85% to 26.19%.

Hydrogen circulation pumps and ejectors in PEMFC systems can both replace each other and be used together to balance the high energy consumption of circulation pumps and the narrow operating range of ejectors. Jenssen et al. [52] proposed that automotive hydrogen management systems typically use a combination of circulation pumps and ejectors to address the issues of low hydrogen inlet flow and poor recirculation performance at low fuel cell output power. Kong et al. [53] compared various pump-ejector coupling modes, finding that the PUE (Pump Upstream of Ejector) mode had the lowest power consumption at 112 W, reducing power by 56.3% compared to the single pump mode and 22.8% compared to the PDE (Pump Downstream of Ejector) mode.

Liang et al. [26] noted that placing the ejector in parallel with the circulation pump combines their advantages, covering all operating conditions and aligning with future development goals.

The ejector, which does not require parasitic power, is more promising for PEMFC systems compared to circulation pumps. Optimizing ejectors is crucial as they can significantly enhance hydrogen supply capacity when operating under effective conditions. While the ejector can significantly enhance hydrogen supply capability under efficient conditions, in practical situations, the secondary flow originates from the waste gas produced after the fuel cell reaction, and its pressure is not always constant [54]. To quantitatively assess the operational efficiency, the entrainment ratio E_R is defined as:

$$E_R = \frac{m_s}{m_p} \tag{1}$$

where m_s and m_p respectively are mass flow rates at secondary and primary inlet.

Current research on the intricate phase-change phenomena within ejectors is very limited. Understanding the varying patterns of phase-change behavior inside ejectors is crucial for their efficient utilization of green energy sources such as hydrogen [55]. In summary, non-equilibrium condensation significantly influences the recirculation performance of the ejector. While the impact of geometric parameters and non-equilibrium condensation on ejector performance has been widely discussed, a comprehensive study on how geometric parameters specifically affect non-equilibrium condensation is still lacking. Therefore, the study established a numerical model considering the phenomenon of non-equilibrium condensation. A comparative analysis was conducted to investigate the relationship between non-equilibrium condensation, ejector structural parameters, and ejector performance. Additionally, the impact of secondary flow pressure fluctuations on ejector structural optimization was innovatively considered, and new parameters were defined to reflect efficiency under varying conditions. Ultimately, the optimal ejector structure was identified.

2. Numerical modeling

2.1. PEMFC system and ejector geometry

As shown in Fig. 1, the PEMFC system is equipped with a high-pressure hydrogen tank, an ejector, a hydrogen recirculation pump, a stack, a water separator, a pressure regulator, a check valve, a purge valve, and two mass flow meters. The system operates in the PUE mode, coupling the circulation pump and the ejector. This configuration effectively expands the system's operational range while significantly reducing overall energy consumption [53]. High-pressure hydrogen from the anode-side tank is depressurized before entering the stack, where it reacts with pure oxygen at the cathode to produce water. Some of this water is carried away by the unreacted oxygen at the cathode, while the remaining water diffuses to the anode and is removed with unreacted hydrogen. On the anode side, liquid water is separated by a water separator. The saturated water vapor and unreacted hydrogen are then passed through the circulation pump and enter the ejector. This process not only ensures suitable humidity for the proton exchange membrane by humidifying the pure hydrogen flow but also enhances hydrogen utilization.

To prevent water vapor accumulation from reducing system efficiency, a purge valve is introduced on the anode side to periodically discharge excess water. Additionally, optimal water management is achieved by adjusting the oxygen flow rate to remove moisture at the cathode, using a water separator to eliminate liquid water from the anode recirculation loop, and employing the ejector to introduce saturated water vapor back into the stack. These actions work together to maintain the proton exchange membrane at optimal humidity levels, thereby preventing excessive dryness, which can lower fuel cell
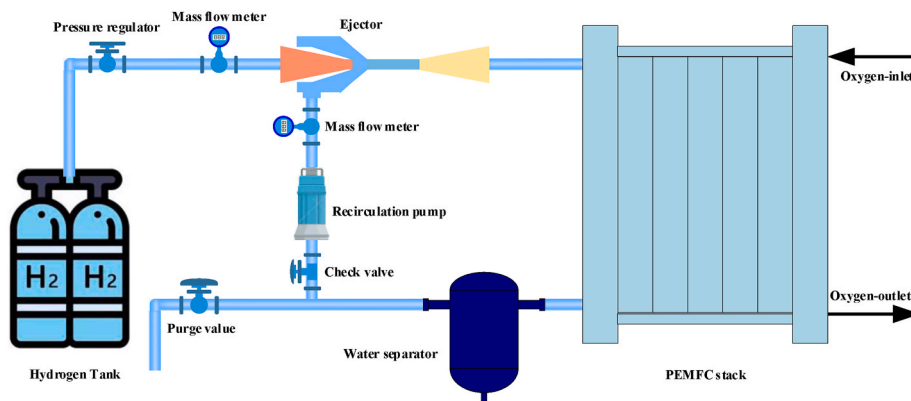
(a) The PEMFC system
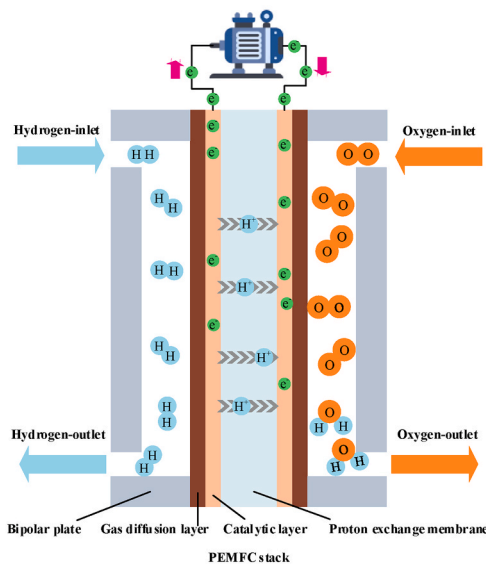
(b) Schematic diagram of the PEMFC stack

Fig. 1. Schematic diagram of the PEMFCs. (a) The PEMFC system (b) Schematic diagram of the PEMFC stack.

efficiency, and excessive moisture, which can cause water blockages and impede gas transport, ultimately reducing cell performance. The operating temperature of the cell is set to 60 °C to balance reaction rates and water management requirements. At lower temperatures, the reaction rate within the cell decreases, the activation energy for electrochemical reactions increases, and the evaporation rate of water slows down, which can lead to excessive accumulation of liquid water and an increased risk of flooding. Conversely, while higher temperatures enhance reaction rates, they also increase the water evaporation rate, potentially causing the proton exchange membrane to become overly dry. This results in increased resistance and membrane dehydration, ultimately affecting system efficiency and the longevity of the
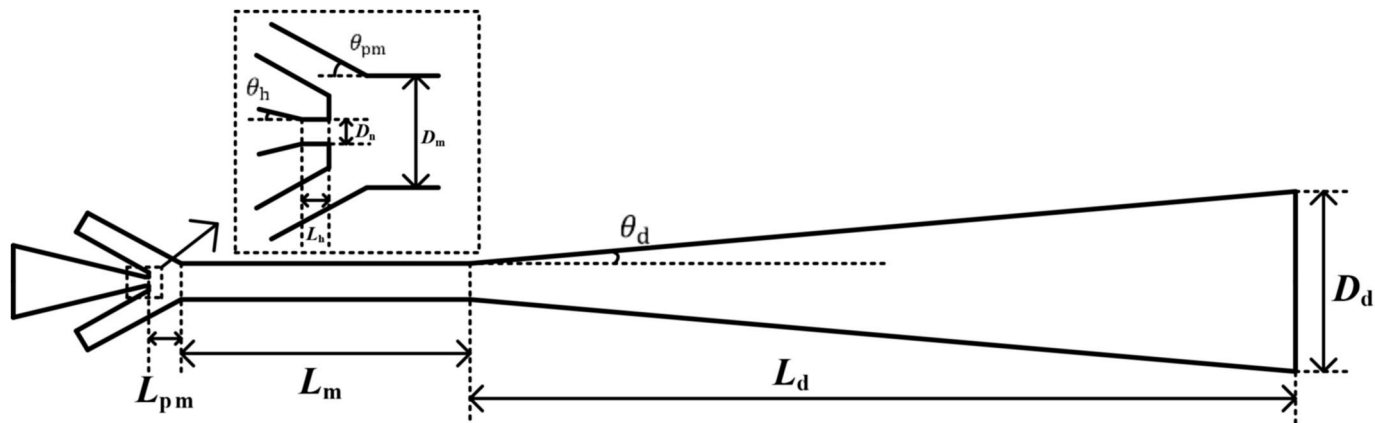

Fig. 2. The baseline ejector in PEMFC system.

membrane [56–58].

As shown in Fig. 2, an ejector consists of a primary nozzle, an entraining entrance, a mixing chamber, and a diffuser. The baseline ejector geometry is modeled as a two-dimensional axisymmetric structure to optimize computational resources [59]. The initial structural parameters, including D_m and θ as key parameters, are listed in Table 2. Table 3 provides the boundary conditions. With a gas-liquid separator installed before the secondary flow inlet of the ejector, it is assumed that all liquid water is removed, leaving only unreacted hydrogen and saturated water vapor to enter the ejector. Consequently, the primary flow consists of pure hydrogen, while the secondary flow is a mixture of hydrogen and saturated water vapor. Since the hydrogen from the high-pressure tank is stored at ambient temperature, the primary flow inlet and outlet temperatures are set to 20 °C. Based on the calculated dew point, the secondary flow inlet temperature is set to 60 °C. The ejector's outlet and secondary flow inlet pressures are estimated from the PEMFC stack's inlet and outlet pressures.

2.2. Numerical scheme

The governing equations are discretized using the finite volume method, and combined with the physical properties and flow characteristics of the working fluid, the model is simplified.

(1) The fluid satisfies the ideal gas state equation;
(2) The inner wall is thermally insulated and non-slip;

The convective term is spatially discretized using the second-order upwind scheme, and the diffusion term is discretized using the central difference method. The inlet boundary condition is defined as a constant total pressure and temperature, while the outlet boundary condition is set as a constant static pressure. In addition, considering the high accuracy of SST k-ω turbulence model [60] in forecasting condensation behavior, it is selected as the viscosity model in the ejector. What's more, a density-based implicit solver is used to calculate the flow area. Furthermore, to calculate non-equilibrium condensation behavior of wet gas flow, the User-defined scalars (UDS) and user-defined functions (UDF) are used. And related parameters are stored in user-defined memory (UDM).

2.3. Mathematical model

Non-equilibrium condensation is an important phase change phenomena in ejector [61]. Therefore, considering this phenomenon in numerical analysis is crucial. A mathematical model considering non-equilibrium condensation is developed to simulate phase change condensation in ejector. In this section, the mathematical foundations of this study will be elaborated.

2.3.1. Wet hydrogen flow conservation equations

The effect of gravity is ignored when the internal control equation is established. And the medium circulating through the hydrogen recirculation ejector is a gas-liquid mixture considering the phase change process. The Navier-Stokes equations are the conservation equations and the continuity, momentum and energy conservation equations are respectively represented as follows.

$$\frac{\partial \rho}{\partial t} + \nabla(\rho \overline{u}) = S_m \tag{2}$$

Table 3
Settings of ejector boundary condition.

Boundary conditions	Pressure (bar)	Temperature (K)	Mass fraction of H2O (−)
Primary flow	3	293.15	0
Secondary flow	1.2	333.15	0.14
Outlet flow	1.25	293.15	–

$$\frac{\partial(\rho \overline{u})}{\partial t} + \nabla(\rho \overline{u_i u_j}) = -\nabla p + \nabla(\overline{\overline{\tau}}) + S_F \tag{3}$$

$$\frac{\partial(\rho E)}{\partial t} + \nabla[\overline{u}(\rho E + p)] = -\nabla\left(\lambda \nabla T - \sum_j h_j J_j + \overline{\overline{\tau}}\,\overline{u}\right) + S_h \tag{4}$$

The fluid is a mixture, so the species transport equation is written as

$$\frac{\partial(\rho Y_j)}{\partial t} + \nabla(\rho \overline{u} Y_j) = -\nabla \overline{D}_j \tag{5}$$

where u, p, ρ and E represent velocity, pressure, density and the total energy respectively. h_j, Y_j and $\overline{D}_j$ represent the enthalpy, mass fraction and diffusion flux of species j respectively. $\overline{\overline{\tau}}$ represents the stress tensor. S_m S_F and S_h represent mass, momentum and energy source terms respectively. S_F, S_m, S_h are designated by

$$S_m = -m_v \tag{6}$$

$$S_F = -m_v u \tag{7}$$

$$S_h = m_v(h - h_{lg}) \tag{8}$$

where h_{lg} and m_v represent the latent heat of condensation and mass generation rate.

The droplet number N and liquid mass fraction Y are written as

$$\frac{\partial(\rho N)}{\partial t} + \nabla(\rho \overline{u} N) = I \tag{9}$$

$$\frac{\partial(\rho_m Y)}{\partial t} + \nabla(\rho_m \overline{u} Y) = m_v \tag{10}$$

where I is the nucleation rate, the subscript m represents the mixture.

2.3.2. The droplet nucleation and growth model

The non-equilibrium condensation process includes nucleation and droplet growth. When the water vapor reaches the saturation state, if the cooling and depressurization continue and no external particles are added, the water vapor does not immediately condense, but becomes supersaturated. After that, the resulting droplets will grow rapidly. Therefore, the liquid phase's mass increase is defined as the droplet mass generation rate m_v, which is given by

$$m_v = \frac{4}{3}\pi\rho_l I r_c^3 + 4\pi\rho_l N r^2 \frac{\partial r}{\partial t} \tag{11}$$

where the subscript l represents the liquid. r and r_c represent the droplet radius and critical radius respectively.

$$r_c = \frac{2\sigma}{p_l RTlnS} \tag{12}$$

Table 2
Detailed data listing of the baseline ejector.

Geometric parameters	D_m	L_m	L_{pm}	θ_d	L_d	θ_h	θ	L_h	D_n
Values (mm)	2.00	16.00	1.80	5.00	45.72	13.50	0	0.25	0.50

where σ, S and R represent liquid surface tension, the super saturation ratio and gas constant.

$$\sigma = 75.67 \times \frac{T_g}{647.3} - 256.889 \times \left(\frac{T_g}{647.3}\right)^2 + 95.928 \times \left(\frac{T_g}{647.3}\right)^3 + 85.27 \tag{13}$$

The homogeneous nucleation rate using the classic nucleation theory and corrected by Kantrowitz [62] is defined by Ref. [63]:

$$I = \frac{q_c}{1+\theta} \frac{\rho_v^2}{\rho_l} \sqrt{\frac{2\sigma}{\pi M_m^3}} exp\left(-\frac{4\pi\sigma r_c^2}{3k_B T}\right) \tag{14}$$

where θ, q_c, and M_m represent non-isothermal correction factor, the condensation factor and water molecular mass respectively. The subscript v represents vapor. k_B represents Boltzmann's constant.

θ is related to the specific heat capacity ratio γ and is given by

$$\theta = \frac{2(\gamma-1)}{\gamma+1} \frac{h_{\text{lg}}}{RT} \left(\frac{h_{\text{lg}}}{RT} - \frac{1}{2}\right) \tag{15}$$

The droplet growth rate $\frac{dr}{dt}$ is given by Ref. [64]:

$$\frac{dr}{dt} = \frac{\lambda(T_s - T)\left(1 - \frac{r_c}{r}\right)}{\rho_l h_{\text{lg}} r \left(\frac{1}{1+2\beta Kn} + 3.78(1-v_0)\frac{Kn}{Pr}\right)} \tag{16}$$

where Pr, λ and Kn represent Prandtl number, thermal conductivity and Knudsen number respectively. the correction factor v_0 is defined by

$$v_0 = \frac{RT_s}{h_{\text{lg}}}\left(\alpha - 0.5 - \frac{2-q_c}{2q_c}\frac{\gamma+1}{2\gamma}\frac{c_p T_s}{h_{\text{lg}}}\right) \tag{17}$$

where $\alpha = 9$.

2.3.3. Visualization of mass transfer

The boundary of the mixing section is used to quantify the level of mixing. And the species quality Φ represents the local mass fraction of the secondary flow [65]. For more efficient analysis, the equipotential line with Φ of 0.9 delineates the boundary between the mixed section and the secondary flow, and the equipotential line with Φ of 0.1 marks the boundary among the mixed section and the primary flow.

The species transfer model is then introduced to enable the visualization of the mass transfer throughout the mixing process. The governing equation is given by

$$\nabla(\rho \vec{v} \Phi) = \Delta \vec{J} + S \tag{18}$$

$$\vec{J} = -\left(\rho D_m + \frac{\mu_T}{S_{\text{Ct}}}\right)\nabla\Phi \tag{19}$$

where S_{Ct}, S and D_m represent turbulent Schmitt number, additional generation rate, and mass diffusion term. The non-dimensional value of S_{Ct} is 0.7 [66].

3. CFD validation

3.1. Grid independence verification

Grid-independent validation was conducted, and the grid is shown in Fig. 3. To guarantee the predictive accuracy of the wet gas model employed, Grid independence was assessed using the grid convergence index (GCI) [67]. The validation of GCI is conducted based on the refinement of error assessment within the framework of Richardson extrapolation theory. The equation is as follows.

$$GCI = \frac{F_s|\varepsilon|}{r^p - 1} \times 100\% \tag{20}$$

where p, r, ε and F_s represent the algorithm's order, proportion of refinement factor, the relative discrepancy between two sets of grids and the safety factor respectively. The value of F_s commonly is 3. A smaller GCI indicates a better grid.

The established CFD model was employed to analyze three grid sets: fine (85,200 cells), medium (74,495 cells) and coarse (57,900 cells). With the outlet pressure as the experimental variable, the results indicate that, concerning the discretization problem in grid calculations, refining the grid does not sufficiently enhance the precision of CFD computations. Therefore, employing 74,495 grids of moderate refinement for further investigation strikes a balance between computational precision and speed.

3.2. Validating via supersonic nozzle

Model validation was conducted to verify the precision of the wet gas model. The dimensions of the nozzle and the grid are depicted in Fig. 4. The operating fluid was moist air, and the inlet and outlet pressures are set to 3 atm and 1 atm, respectively. To balance between computation speed and computational costs, a grid independence verification was conducted using a method similar to that in Section 3.1. The pressure along the nozzle wall for various Φ^{in} is depicted in Fig. 5. It is evident that the computational fluid mechanics simulation results closely match the experimental results, indicating that the model is able to effectively anticipate nucleation and growth processes.

3.3. Validating via hydrogen ejector

Based on the experimental data provided by K. Nikiforow [68], the ejector's geometric dimensions can be obtained. The two-dimensional axisymmetric computational domain of the ejector and grid generation are illustrated in Fig. 3. The grid refinement was implemented on the inner surface and the throat to enhance computational accuracy. Four cases were chosen for validation, where $P_{p,in}$ values were set as 3, 4, 5, and 6 bar, while secondary inlet pressure $P_s = 1.2$ bar, and outlet pressure $p_{out} = 1.25$ bar. The comparison between the simulated results of the two models for m_s and the experimental data is shown in Fig. 6. According to the results, m_p predicted by the two models are very similar, with both models maintaining essentially the same status. However, a significant discrepancy exists between m_s predicted by the two models. Generally, m_s predicted by dry gas is higher.

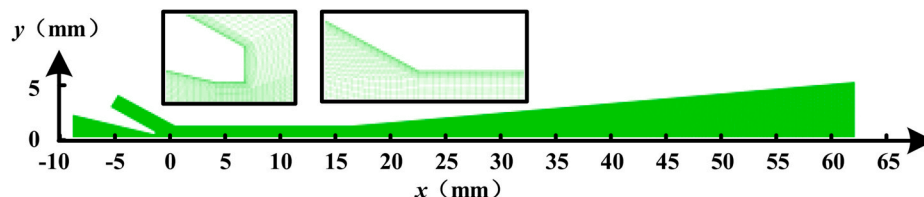Using the mean relative error (MRE) as an evaluation metric, the

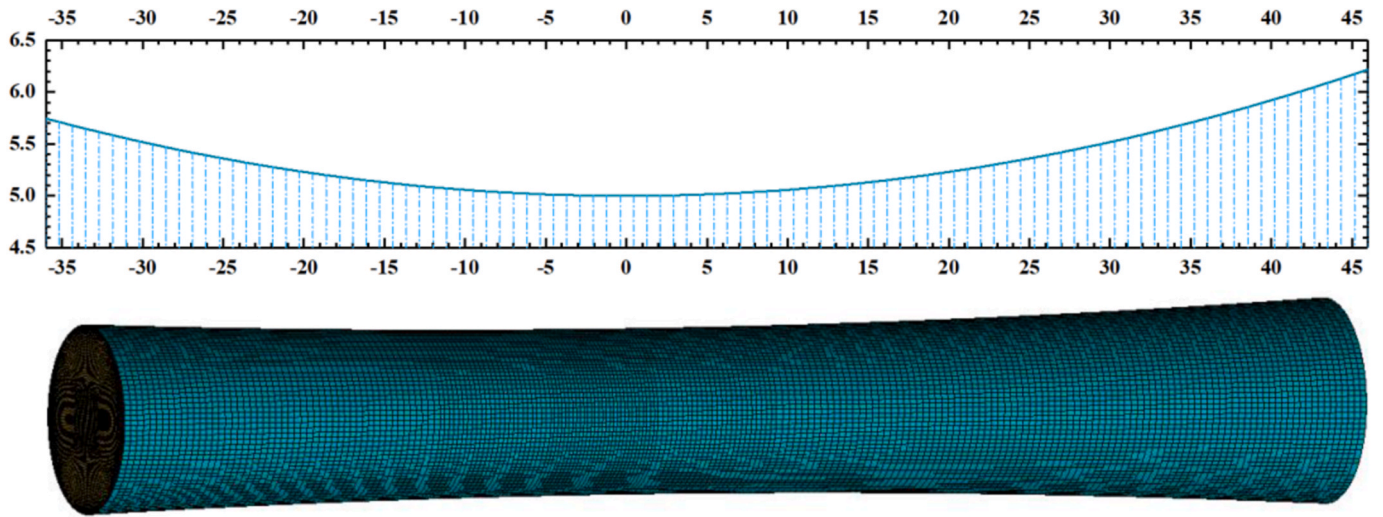**Fig. 3.** Geometry and mesh particulars.
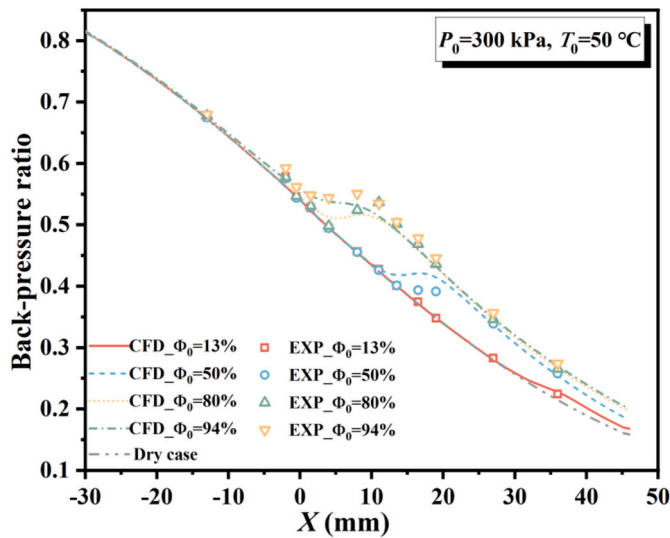
Fig. 4. Dimensions and grid schematic.

Fig. 5. Comparison of CFD and experimental wall pressure data with various Φ^{in}.

Fig. 6. Comparion of m_s under two models.

difference between the predictive accuracy of the experimental results and the two models is depicted in Fig. 7. The formula for calculating the MRE is as follows:

$$MRE = \frac{1}{n} \sum_{i=1}^{n} \left| \frac{(y_i - \overline{y_i})}{y_i} \right| \tag{21}$$

where $\overline{y_i}$ and y_i represent simulated and experimental data, respectively. n represents the data volume.

The results demonstrate a significantly higher MRE between experimental data and dry gas model, reaching 30.17%, whereas wet gas shows an MRE of only 2.53% with experimental data. This suggests that, in predicting non-equilibrium condensation behavior within the ejector, wet gas model exhibits substantial advantages, presenting higher predictive capabilities and accuracy. Consequently, the mathematical model established is applicable for simulating non-equilibrium condensation phenomena within the ejector.
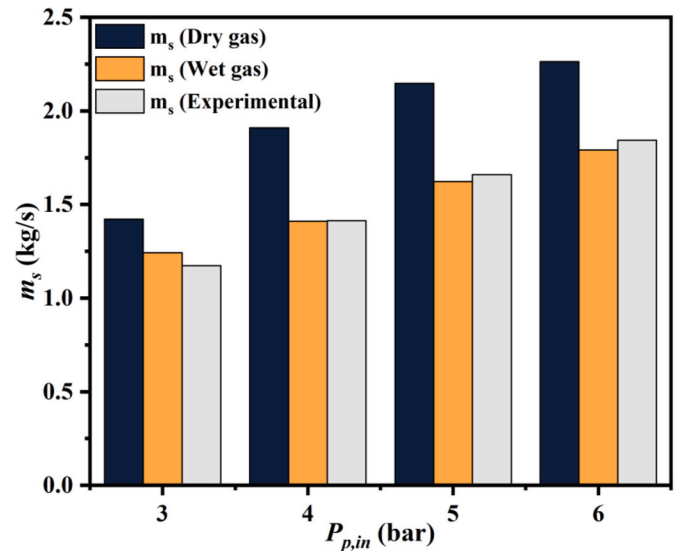
4. Results and discussion

4.1. Non-equilibrium condensation

Fig. 8 shows I and $\frac{dr}{dt}$ distribution of the wet gas model when $P_{p,in} = 3$ bar, $P_{s,in} = 1.2$ bar and $P_{out} = 1.25$ bar. Droplet nucleation mainly occurs in the mixing chamber, and I gradually decreases from the center towards both sides, achieving a peak of 1.23×10^{27} m^{-3}·s^{-1}. On the other hand, droplet growth mainly takes place in mixing chamber, continuing until near the entrance of the diffuser, where it stops. The maximum I is 7.81×10^{-4} m/s in this region.

The Mach number and pressure of two models are shown in Fig. 9. It can be observed that the performance of two models exhibits similar trends in terms of Mach number and pressure. In dry gas model, the Mach number increases maximally to 1.275 after passing through the nozzle, with the pressure dropping to a minimum of 1.079 bar. Similarly, in the wet gas model, the Mach number increases maximally to 1.274, with the pressure dropping to a minimum of 1.081 bar. From the results, it is apparent that dry gas model overestimates the pressure drop and velocity increase at the nozzle outlet. Considering the crucial effect
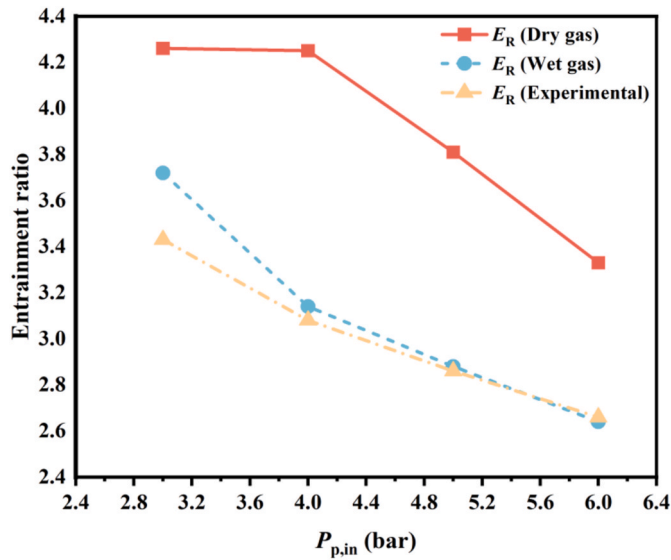
Fig. 7. Comparison of E_R under two models with experimental data.

of the mixing chamber, the pressure and Mach number variation on the axis are analyzed. Both the pressure and Mach number show oscillatory changes in the mixing chamber, which means there are shock waves. On the axial line, the pressure obtained from simulations using dry gas model is significantly lower, while the Mach number is notably higher. The reason for this phenomenon is that during the droplet formation process, the droplets absorb energy from the gas-phase flow, releasing latent heat, which reheats the mixed flow, causing a decrease in flow velocity and an increase in pressure.

From the above results, the maximum pressure drop obtained by the wet gas model is 1.919 bar, while dry gas model's maximum pressure drop is 1.921 bar. This implies that dry gas model exaggerates the pressure difference. As the pressure difference increases, the entrainment capability of the primary flow is enhanced. Undoubtedly, the false exaggeration of entrainment performance by dry gas model has occurred. In other words, the occurrence of non-equilibrium condensation phenomena is undesirable.

4.2. Geometric optimization

The ejector's geometric design significantly influences the recirculation efficiency. Key parameters include the throat diameter (D_m) and the nozzle divergence angle (θ). Table 4 shows the ranges of values for D_m and θ in the experiments.

4.2.1. Diameter of constant-area mixing chamber

D_m is a critical geometric parameter for the hydrogen recirculation ejector. Numerical simulation sets D_m in the range of 2.0 mm–3.0 mm.

Fig. 10 a) demonstrates the distribution of droplet nucleation and growth rates under various D_m. As the D_m increases, both the distribution range and peak value of droplet nucleation decrease to some extent. When the D_m is 2.20, 2.40, 2.60, 2.65, and 2.80 mm respectively, the peak values of droplet nucleation rate are 9.55×10^{26} m$^{-3} \cdot$s^{-1}, 8.91×10^{26} m$^{-3} \cdot$s^{-1}, 8.13×10^{26} m$^{-3} \cdot$s^{-1}, 7.94×10^{26} m$^{-3} \cdot$s^{-1} and 7.08×10^{26} m$^{-3} \cdot$s^{-1}. The peak values of I decrease in a relatively stable manner as the diameter decreases, without significant abrupt decreases occurring during the reduction process. For $\frac{dr}{dt}$, when D_m increases from 2.00 mm to 2.60 mm, both the magnitude and peak value of $\frac{dr}{dt}$ decrease slightly. In the case of a 0.20 mm span, as the D_m increases from 2.00 mm to 2.60 mm, the peak values of the droplet growth rates are 7.81×10^{-4} m/s, 7.77×10^{-4} m/s, 6.97×10^{-4} m/s, 5.56×10^{-4} m/s, with corresponding decreases of 0.04×10^{-4} m/s, 0.80×10^{-4} m/s, and 1.41×10^{-4} m/s, respectively. However, as the diameter increases to 2.65 mm, the occurrence range of droplet growth significantly decreases, and the maximum value of $\frac{dr}{dt}$ decreases substantially to 3.56×10^{-4} m/s. With an increase in diameter of only 0.05 mm, the maximum value of $\frac{dr}{dt}$ decreases by 2.00×10^{-4} m/s. To provide a more intuitive and clear comparison of the rate of change of the droplet growth rate under different D$_m$, a new parameter, the sensitivity of droplet growth rate on D_m, is defined as:

$$R_{1,2} = \frac{\left[\left(\frac{dr}{dt}\right)_1 - \left(\frac{dr}{dt}\right)_2\right] / \left(\frac{dr}{dt}\right)_1}{|D_{m1} - D_{m2}|} \tag{22}$$

where 1 and 2 represent different values of D_m.

Through calculations, it can be determined that when the D_m increases from 2.00 mm to 2.60 mm, the average decrease rate of the droplet growth rate is 48.0% per millimeter. However, when D_m increases from 2.60 mm to 2.65 mm, the average decrease of $\frac{dr}{dt}$ is 719.4% per millimeter. This indicates that this range of diameter variation is a sensitive area to changes in non-equilibrium condensation intensity. When the diameter reaches 2.80 mm, the occurrence range of droplet growth decreases to a negligible level, and the peak value of $\frac{dr}{dt}$ is only 1.23×10^{-4} m/s, indicating that droplet growth almost ceases. This illustrates that an increase in D_m leads to a decrease in non-equilibrium condensation intensity within the ejector, and there exists a sensitive range where non-equilibrium condensation intensity undergoes drastic changes. The presence of this sensitive range has a beneficial impact.

Fig. 10 b) illustrates the distribution of the liquid phase mass fraction along the axial direction for various D_m. Before the axial position $x = 5.0$ mm, the liquid phase mass fractions under different D_m are negligible. This is because the phenomenon of droplet growth mainly occurs in the central portion of the mixing chamber, with minimal droplet growth occurring at the front end of the chamber. However, within the axial range from $x = 5.00$ mm to $x = 16.00$ mm, the liquid phase mass fraction decreases with an increase in D_m. Specifically, as D_m increases from 2.20 mm to 2.60 mm, the reduction in the liquid phase mass fraction is
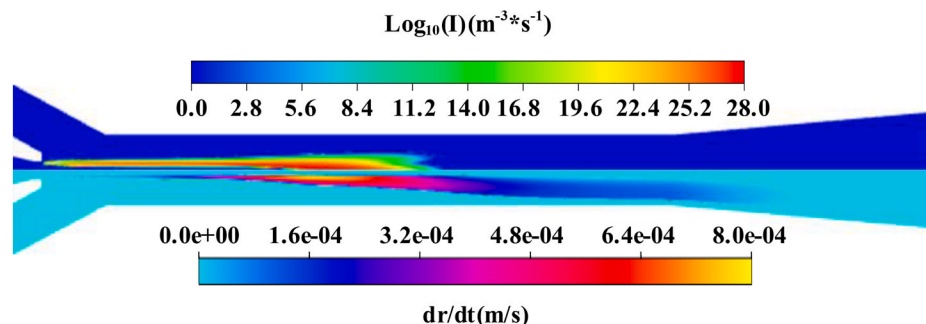

Fig. 8. Distribution of I and $\frac{dr}{dt}$ under standard operating conditions.

a) Pressure distribution in the ejector.

b) Mach number distribution in the ejector.

c) Pressure on the axis.

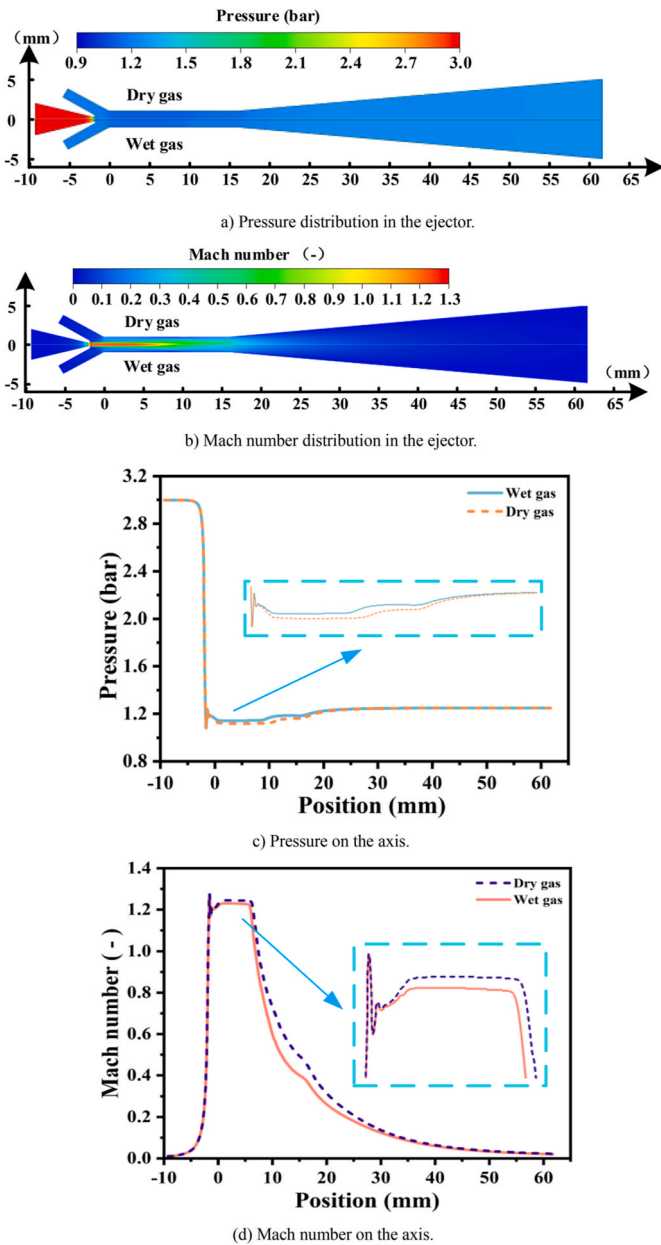(d) Mach number on the axis.

Fig. 9. Comparisons of pressure and Mach number between two models. a) Pressure distribution in the ejector. b) Mach number distribution in the ejector. c) Pressure on the axis. (d) Mach number on the axis.

Table 4
The structure parameter and its value range.

Structural parameter	Range
Ejector throat diameter D_m (mm)	2.00, 2.20, 2.30, 2.40, 2.50, 2.55, 2.60, 2.65, 2.70, 2.80, 3.00
Nozzle divergent angle θ (°)	3.0, 6.0, 7.0, 8.0, 9.0, 10.0, 11.0, 11.5, 12.5, 13.0, 14.0, 15.0

relatively stable, followed by a substantial decrease. After increasing the diameter to 2.80 mm, the liquid phase mass fraction for each cross-section almost ceases to increase, maintaining at a very low level, indicating the absence of droplet growth phenomena at this point. This result further visually confirms the above conclusion: the larger D_m is, the lower the intensity of non-equilibrium condensation is. Moreover, after increasing the diameter to 2.60 mm, the non-equilibrium

condensation phenomenon is nearly neglected, and at this point, the dry and wet gas models no longer exhibit significant differences.

Fig. 11 illustrates the pressure distribution under different D_m for two models. The results indicate that when the D_m is 3.00 mm, the pressure distributions of two models are most similar, with the lowest pressure inside the ejector being 1.086 bar in both cases. The wet gas model exhibits lower sensitivity to changes in D_m. When D_m increases from 2.00 mm to 3.00 mm, the lowest pressure for the dry and wet gas models increases by 0.007 and 0.005 bar, respectively.

Fig. 12 presents the results of the visual analysis. First, the axial direction aligns with the X-axis, while the radial direction aligns with the Y-axis. From Fig. 12 a), it can be observed that with the increase of D_m, the primary mixing boundary $\Phi_{0.1}$ and the secondary mixing boundary $\Phi_{0.9}$ gradually keep away from each other. $\Phi_{0.9}$ in the radial direction generally shows an increasing trend with the increase of D_m, reaching its maximum at $D_m = 2.65$ mm before decreasing. Fig. 12 b) and c) respectively illustrate the pressure distribution along $\Phi_{0.1}$, and the pressure distribution along $\Phi_{0.9}$.

Fig. 13 comprehensively analyzes the impact of the variation in D_m on ejector performance from multiple perspectives. Given that m_p remains nearly constant under different experimental conditions, E_R is directly related to m_s. Therefore, a new parameter, the secondary flow intensity Q^*, is defined as:

$$Q^* = \left(\frac{D_m}{D_n}\right)^2 \cdot \left(\frac{\Delta P}{P_{p,in}}\right)^{\frac{1}{3}} \tag{23}$$

where ΔP is the Differential pressure between the center of the entrance to the mixing chamber and $P_{s,in}$.

From Fig. 13 a), with the increase in D_m, m_s in dry gas model increases first and then decreases, reaching its maximum at a diameter of 2.5 mm. In wet gas model, besides reaching the first peak at a diameter of 2.5 mm, m_s begins to experience a second increase as the diameter further grows to 2.6 mm. Overall, when D_m is below 2.7 mm, wet gas model exhibits a significantly lower m_s. However, after the diameter increases to 2.7 mm, the two are almost the same. Fig. 13 b) illustrates the change in E_R with D_m for two models. With the increase in D_m, E_R of dry gas model initially increases and then decreases, reaching a peak value of 4.60 as $D_m = 2.4$ mm. Notably, wet gas model shows two peaks, occurring at diameters of 2.5 mm and 2.65 mm, with E_R reaching 4.21 and 4.24, respectively. An analysis of the unexpected decrease in $P_{s,in}$ was conducted. The results in Fig. 13 c) indicate that as D_m increases, the rate of decrease in E_R gradually increases. when D_m is 2.40, 2.50, 2.55, 2.60, 2.65, and 2.70 mm, the entrainment ratio decreases by 19.0%, 22.7%, 23.5%, 23.4%, 30.8%, and 36.0%, respectively. This implies that smaller D_m possess a stronger ability to resist disturbances in the pressure of the secondary flow. Therefore, the optimal choice is $D_m = 2.4$ mm.

4.2.2. Nozzle divergent angle

Numerical simulations are conducted for θ, with the range set between 3.0° and 15.0°. Based on Fig. 14 a), as θ increases, the intensity of droplet nucleation exhibits a relatively stable decreasing trend. When θ increases from 3.0° to 14.0°, the maximum value of I decreases only from 9.06×10^{26} m^{-3}·s^{-1} to 7.62×10^{26} m^{-3}·s^{-1}. When θ increases from 3.0° to 10.0°, the reduction in the distribution range of droplet growth is relatively small. The peak value of $\frac{dr}{dt}$ decreases from 6.93×10^{-4} m/s to 5.50×10^{-4} m/s, the decrease is 1.44×10^{-4} m/s, representing the average reduction rate of 3.0% per degree. However, when θ increases from 10.0° to 11.0°, the distribution range of droplet growth significantly decreases, and the peak value of $\frac{dr}{dt}$ decreases to 1.03×10^{-4} m/s, the decrease is 4.47×10^{-4} m/s, representing the average reduction rate of 81.2% per degree. Continuing to increase θ, the distribution range of droplet growth becomes negligible. The results indicate that non-equilibrium condensation's strength decreases as θ increases, and
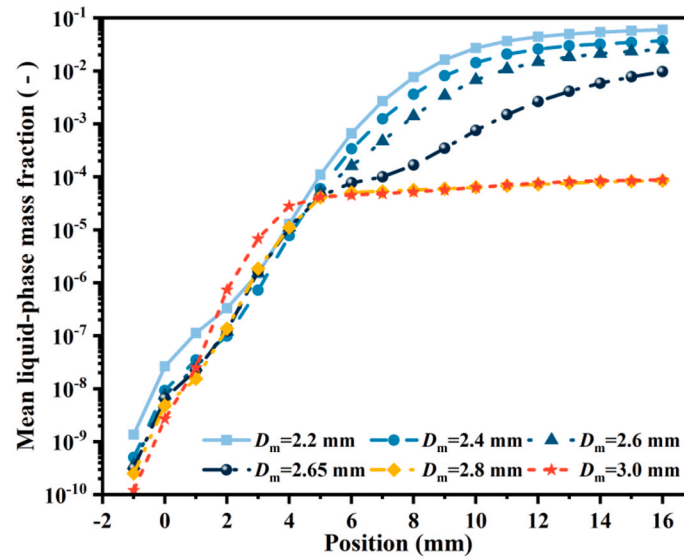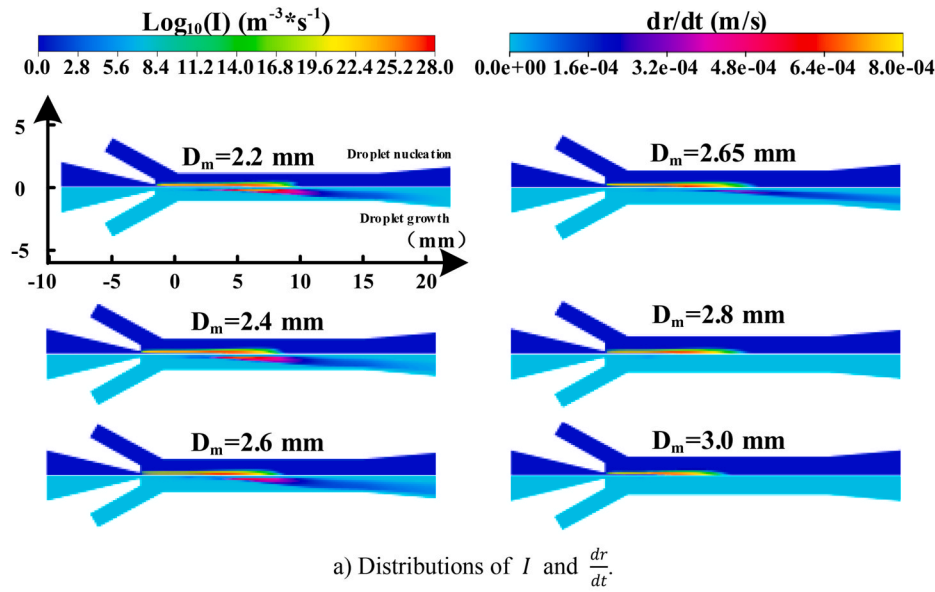
a) Distributions of I and $\frac{dr}{dt}$.

b) Axial profile of liquid phase mass fraction.

Fig. 10. Comparison of non-equilibrium condensation intensity with various D_m. a) Distributions of I and $\frac{dr}{dt}$. b) Axial profile of liquid phase mass fraction.

there exists a sensitive range. Fig. 14 b) illustrates the pressure distributions under two models for different θ. The pressure variation primarily concentrates near the nozzle exit. As θ is below 11.0°, the pressure drop near the nozzle exit is significantly greater in dry gas model. However, when θ exceeds 11.0°, pressure distribution exhibits minimal variance between two models, this is because of the significant reduction in non-equilibrium condensation intensity.

Fig. 14 c) illustrates the liquid phase mass fraction along the axial direction for different θ. The axial position x = 5.0 mm is a dividing line, the liquid phase mass fraction can be neglected before this point. Beyond this point, with the increase in θ, the liquid phase mass fraction along the axial direction decreases. Notably, as the angle increases from 6.0° to 10.0°, the reduction in the liquid phase mass fraction remains relatively stable, followed by a substantial decrease. This result further demonstrates that a larger θ corresponds to a lower non-equilibrium condensation intensity.

Fig. 15 presents the visual analysis results for different θ. From Fig. 15 a), the variation in θ has little influence on the boundary length.

Fig. 15 b) and 15 c) depict the pressure distribution along $\Phi_{0.9}$ and $\Phi_{0.1}$, respectively. In the mixing chamber, when θ is below 11.0°, the pressure distribution on the boundaries exhibits a decreasing trend with increasing θ. However, when θ exceeds 11.0°, the pressure distribution along the boundaries is insensitive to change in θ.

Fig. 16 illustrates the impact of θ on E_R. Fig. 16 a) presents E_R for two models, and as θ increases, both of E_R initially increase and then decrease. Specifically, E_R reaches its peak value of 4.657 for dry gas model when $\theta = 6°$, and 4.565 for wet gas model when $\theta = 11.0°$. And when θ exceeds 11.0°, the E_R obtained from two models become very close. Fig. 16 b) investigates the anti-interference ability of $P_{s,in}$ fluctuations under different θ. The results indicate that as $\theta = 11.0°$, 12.0°, 13.0°, and 14.0°, the E_R decreases by 18.9%, 19.2%, 19.0%, and 19.1%, respectively, which indicates that θ is not the key parameter affecting the ejector's anti-interference ability to secondary flow pressure fluctuations. Therefore, based on $D_m = 2.40$ mm, the optimal choice is $\theta = 11.0°$.
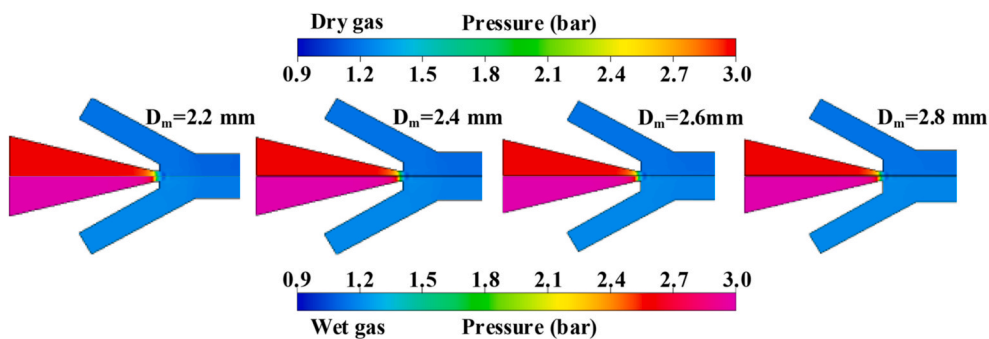
a) Pressure distributions of wet and dry gas.
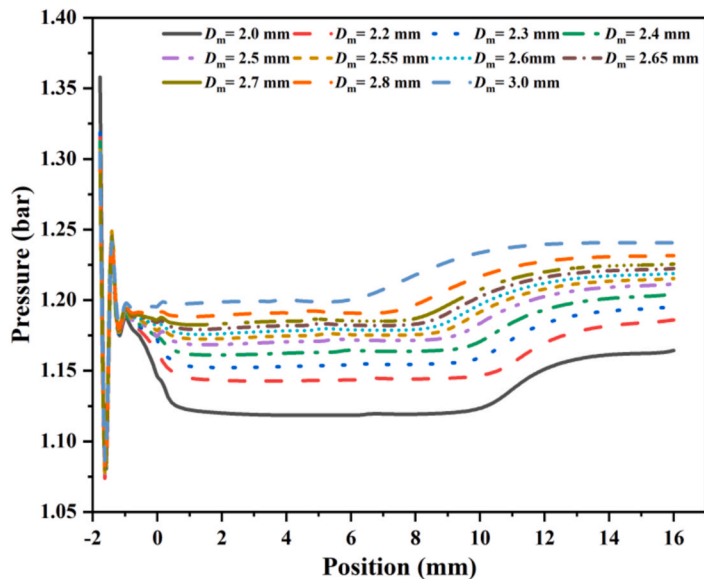
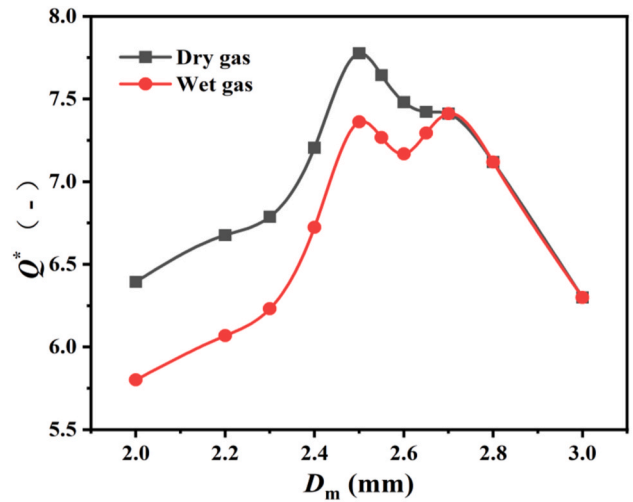**b)** Pressure distribution of dry gas on the axis.
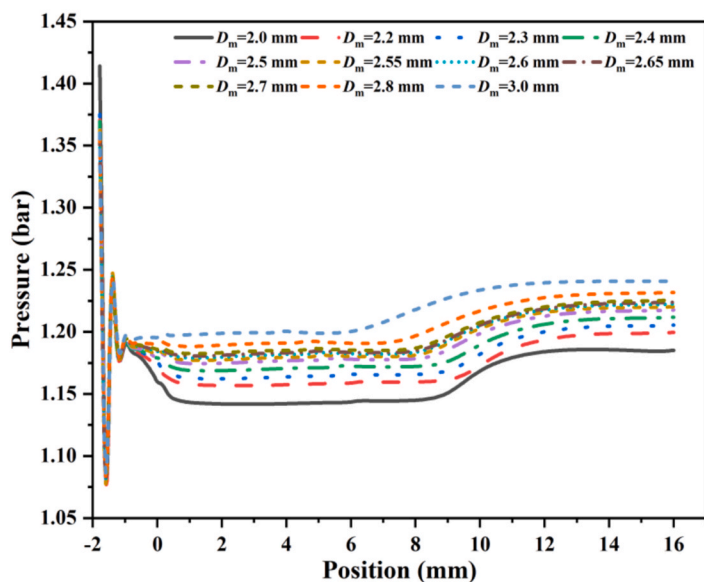
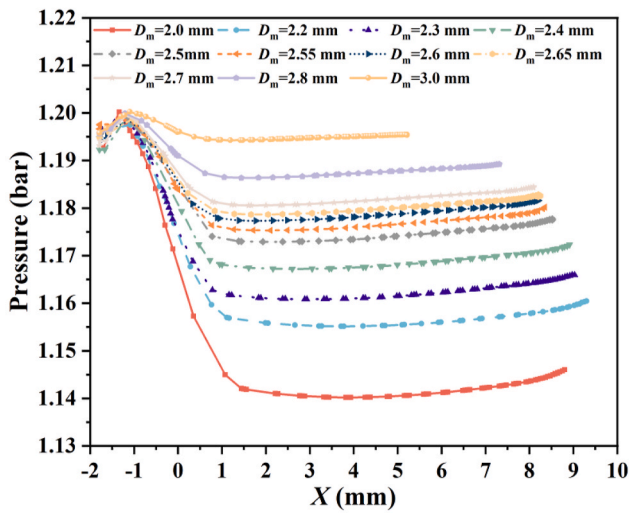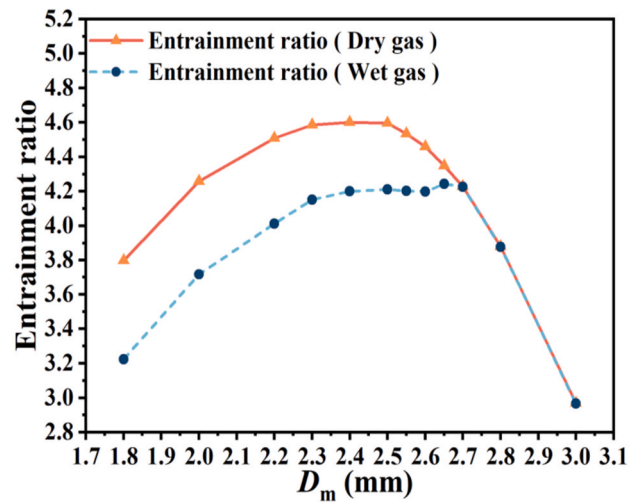**c)** Pressure distribution of wet gas on the axis.

Fig. 11. Comparisons of pressure between wet gas and dry gas at different mixing chamber diameter. a) Pressure distributions of wet and dry gas. **b)** Pressure distribution of dry gas on the axis. **c)** Pressure distribution of wet gas on the axis.
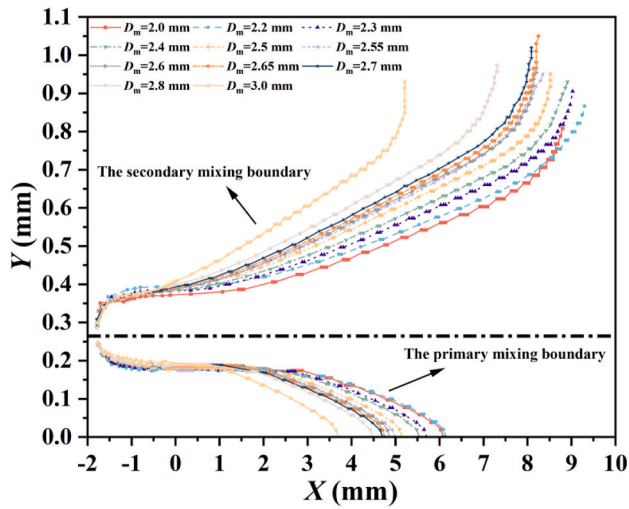
a) Comparison of boundaries at different D_m.
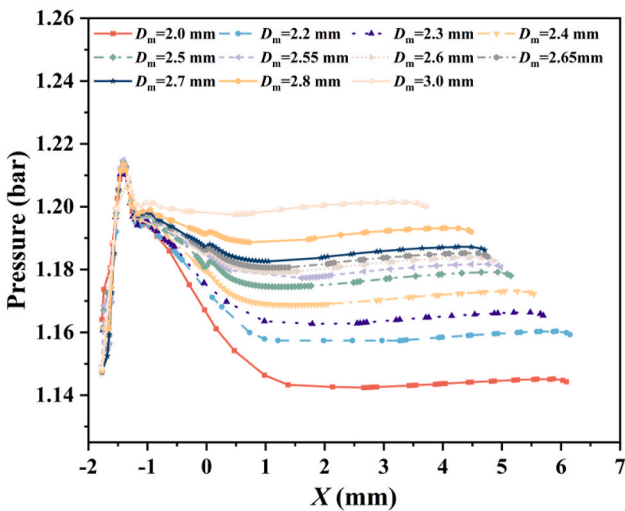

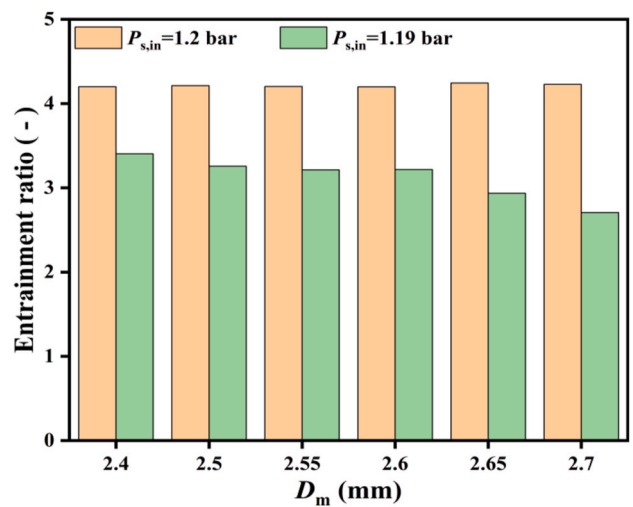a) Effect of D_m on the Q^*

b) Pressure distribution on the primary mixing boundary.


b) Effect of D_m on E_R

c) Pressure distribution on the secondary mixing boundary.

c) Effect of $P_{s,in}$ on E_R under different D_m

Fig. 12. The boundaries of the mixing section and its pressure distribution. a) Comparison of boundaries at different D_m. b) Pressure distribution on the primary mixing boundary. c) Pressure distribution on the secondary mixing boundary.

Fig. 13. Effect of D_m on ejector performance. a) Effect of D_m on the Q^* b) Effect of D_m on E_R c) Effect of $P_{s,in}$ on E_R under different D_m.
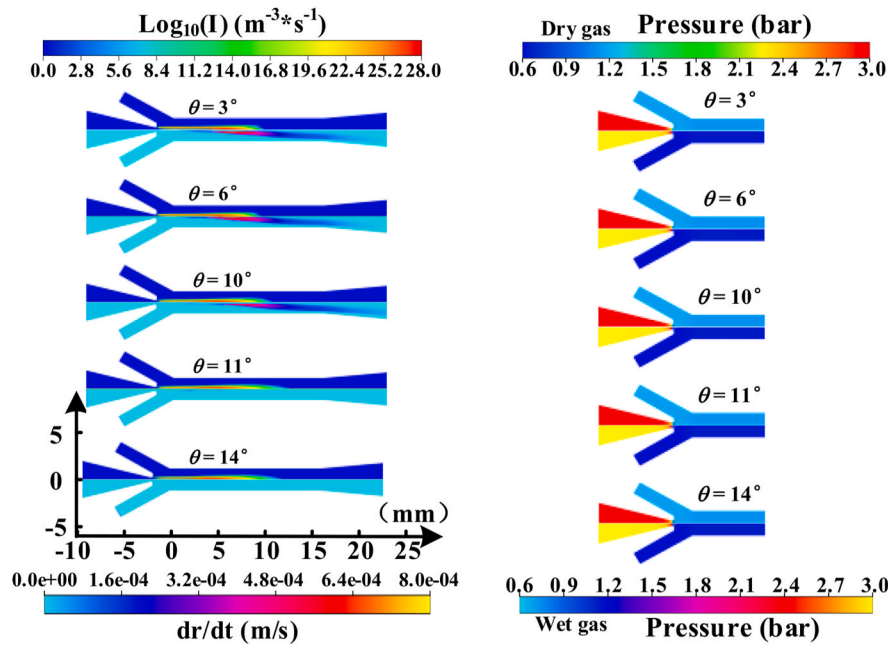
a) Distribution of I and $\frac{dr}{dt}$ b) Comparisons of pressure between two models
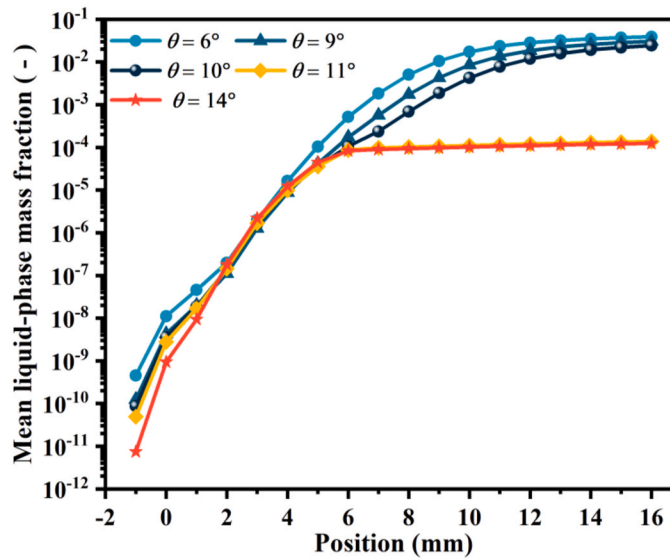
c) Axial distribution of liquid phase mass fraction.

Fig. 14. Comparison of flow characteristics in the ejector at different θ. a) Distribution of I and $\frac{dr}{dt}$ b) Comparisons of pressure between two models c) Axial distribution of liquid phase mass fraction.

4.3. Comparative analysis

A comparative analysis of performance between the optimized and baseline ejectors was conducted. Fig. 17 depicts E_R before and after optimization under different $P_{s,in}$. When $P_{s,in}$ decreases to 1.190 bar, the optimized ejector still exhibits good performance. However, when $P_{s,in}$ drops to 1.185 bar, there is no significant difference in the entrainment performance between the ejector before and after optimization. It can be predicted that further reduction in $P_{s,in}$ may even lead to inferior performance of the optimized ejector compared to the baseline ejector. This underscores the importance of our work: while structural optimization of the ejector effectively enhances efficiency near the operating point, it may not be advantageous for other operating conditions. Particularly,

when the actual operating environment involves significant fluctuations and large amplitudes in $P_{s,in}$, this aspect must be considered. Specific analysis results are as follows: when $P_{s,in}$ is 1.200 bar, 1.195 bar, 1.190 bar, and 1.185 bar, the optimized ejector, compared to the baseline ejector, shows performance improvements of 22.8%, 17.2%, 10.2%, and 2.2%. Considering that the optimization effect is negligible as $P_{s,in}$ is 1.185 bar, the effective optimization range is considered to be from 1.190 bar to 1.200 bar. The maximum optimization effect occurs when $P_{s,in}$ is 1.200 bar, with a 22.8% improvement. On average, the entire effective range experiences a 16.7% improvement. In summary, within the effective operating range of 1.190 bar–1.200 bar, the optimized ejector demonstrates higher E_R and stronger resistance to interference from fluctuations in $P_{s,in}$. However, continued increase in the
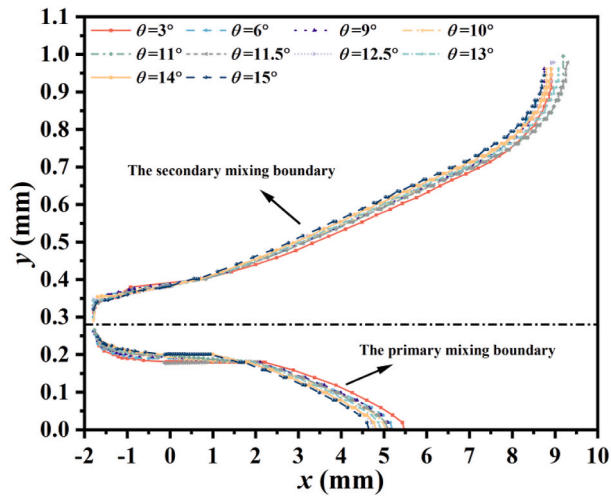
a) Comparison of boundaries for different θ.
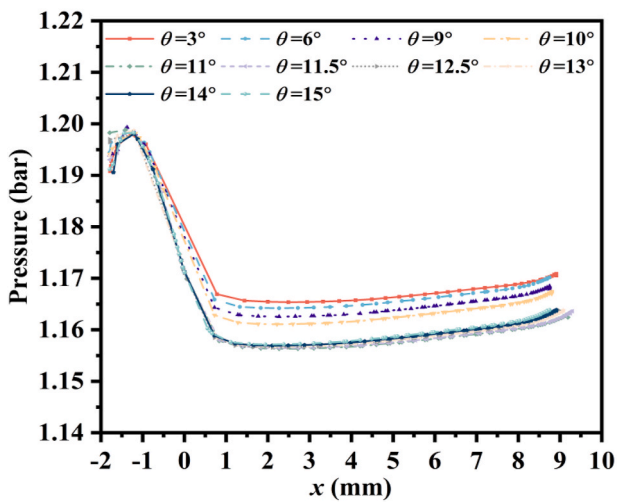
b) Pressure distribution on the secondary mixing boundary.
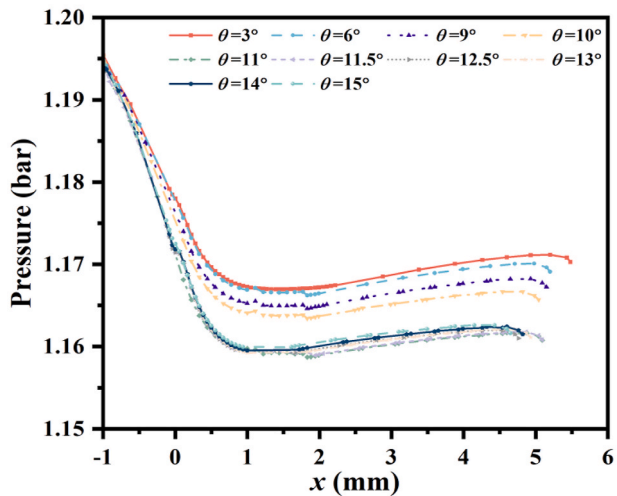
c) Pressure distribution on the primary mixing boundary.

Fig. 15. The boundaries of the mixing section and its pressure distribution. a) Comparison of boundaries for different θ. b) Pressure distribution on the secondary mixing boundary. c) Pressure distribution on the primary mixing boundary.
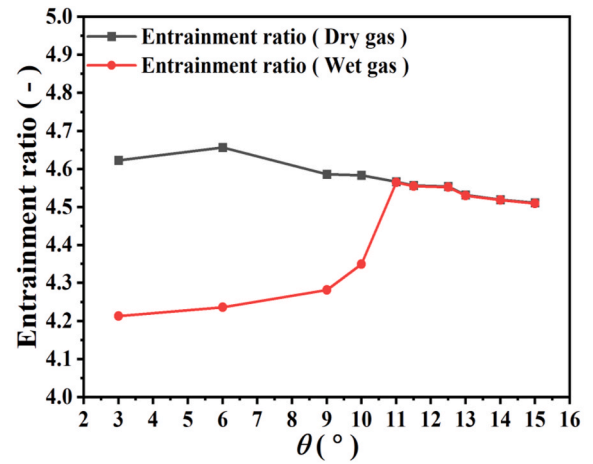
a) Effect of θ on E_R
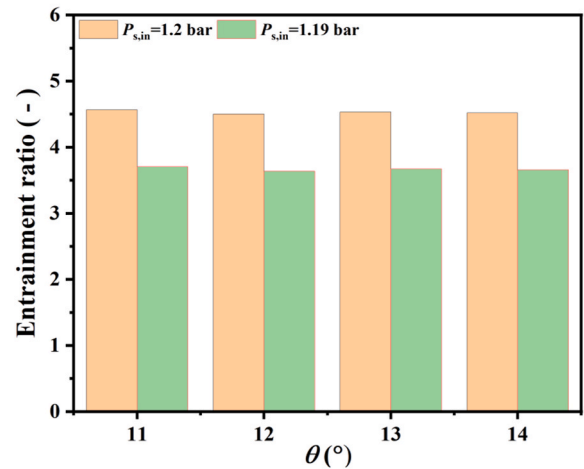
b) Effect of $P_{s,in}$ on E_R under different D_m

Fig. 16. Effect of θ on ejector performance. a) Effect of θ on E_R b) Effect of $P_{s,in}$ on E_R under different D_m.

Fig. 17. Comparison of E_R between optimized and baseline ejectors.

disturbance caused by $P_{s,in}$ can result in deterioration in the performance of the optimized ejector.

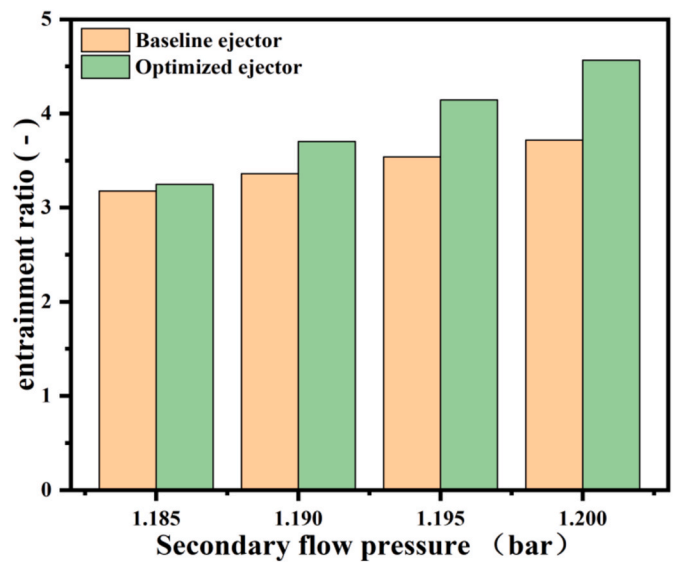The energy consumption of the optimized PEMFC system is also analyzed. Enhancing the entrainment capability of the ejector can reduce the parasitic power from the circulation pump, thereby improving the overall system efficiency. The power reduction rate η_E is defined as:

$$\eta_E = \frac{E_p' - E_p}{E_p'} \times 100\% \tag{24}$$

where E_p' and E_p represent the parasitic power of the circulation pump before and after optimization, respectively. According to the study by Kong et al. [53], there is a linear relationship between the entrainment ratio of the ejector and the parasitic power of the circulation pump under the PUE mode. The relationship is given by the following equation:

$$E_p = 256 - 38.42E_R \tag{25}$$

Based on the above formulas, it can be calculated that the power reduction achieved by coupling the circulation pump with the ejector in the PUE mode is 55.80% compared to the single hydrogen pump mode. This result is highly consistent with the conclusions drawn by Kong et al. Furthermore, using the optimized ejector compared to the baseline ejector results in an additional power reduction of 28.78%, highlighting the energy-saving advantages of the optimization.

5. Conclusions

Hydrogen recirculation ejector require no additional energy supply, effectively enhancing fuel efficiency and reducing resource waste. Most importantly, the ejector is environmentally friendly, providing a sustainable solution for clean energy applications by minimizing hydrogen emissions. To optimize the ejector to the fullest extent, a CFD model for a hydrogen recirculation ejector considering non-equilibrium condensation phenomena is established. Provided new insights for optimizing the ejector's geometric structure. The following are the conclusions.

1. The occurrence of non-equilibrium condensation led to elevated temperature and pressure within the primary flow, resulting in a decrease in pressure difference during the mixing process. This further weakened the entrainment capability of the primary flow, adversely affecting the performance of the ejector.
2. As D_m increases, the strength of non-equilibrium condensation gradually decreases, significantly reducing when the diameter reaches 2.65 mm. The E_R of the wet gas model is smaller, but as D_m increases, the difference in E_R between two models rapidly diminishes, both exhibiting a trend of initially increasing and then decreasing. Within the diameter range of 2.4 mm–2.7 mm, E_R remains insensitive to diameter changes and consistently maintains a high level. Larger diameters make E_R more sensitive to fluctuations in $P_{s,in}$. Therefore, the optimal value for D_m is chosen as 2.4 mm.
3. As θ increases, the trend of non-equilibrium condensation strength and E_R for both models is similar to that observed with increasing D_m. When θ reaches 11°, there is a significant decrease in strength of non-equilibrium condensation. When the range of θ is between 11° and 14°, E_R remains insensitive to angle changes and consistently maintains a high level. The change in θ has little impact on the sensitivity of E_R to fluctuations in $P_{s,in}$. Therefore, the optimal geometric dimensions are chosen as D_m of 2.4 mm and a nozzle divergence angle of 11°.
4. The E_R of the ejector after structural optimization exhibited a maximum improvement of 22.8%, and an average improvement of 16.7% across the entire effective operating range. Compared to the single hydrogen pump mode, the PUE mode reduces power by 55.80%, and the optimized ejector further reduces power by 28.78%

compared to the baseline ejector. However, beyond this effective operating range, the performance of the optimized ejector deteriorates rapidly.

This study offers a new perspective for optimizing the ejector. Future research efforts could focus on elucidating the fundamental mechanisms underlying the complex flow dynamics and expanding the effective operational range of the ejector.

CRediT authorship contribution statement

Hongbing Ding: Writing – original draft, Methodology, Funding acquisition, Formal analysis, Conceptualization. **Panpan Zhang:** Writing – review & editing, Methodology, Investigation, Formal analysis. **Yuanyuan Dong:** Writing – review & editing, Methodology, Formal analysis. **Yan Yang:** Writing – review & editing, Supervision, Methodology, Investigation, Formal analysis, Conceptualization.

Declaration of competing interest

The authors declare that they have no known competing financial interests or personal relationships that could have appeared to influence the work reported in this paper.

Acknowledgement

References

[1] K. Jiao, J. Xuan, Q. Du, et al., Designing the next generation of proton-exchange membrane fuel cells, Nature 595 (7867) (2021) 361–369.
[2] Y. He, Y. Zhou, J. Yuan, et al., Transformation towards a carbon-neutral residential community with hydrogen economy and advanced energy management strategies, Energy Convers. Manag. 249 (2021) 114834.
[3] E. Lakzian, S. Yazdani, F. Salmani, et al., Supersonic separation towards sustainable gas removal and carbon capture, Prog. Energy Combust. Sci. 103 (2024) 101158.
[4] Y. Wang, D.F.R. Diaz, K.S. Chen, et al., Materials, technological status, and fundamentals of PEM fuel cells–a review, Mater. Today 32 (2020) 178–203.
[5] J. Shen, Z. Tu, S.H. Chan, Enhancement of mass transfer in a proton exchange membrane fuel cell with blockage in the flow channel, Appl. Therm. Eng. 149 (2019) 1408–1418.
[6] H. Chang, C. Duan, X. Xu, et al., Technical performance analysis of a micro-combined cooling, heating and power system based on solar energy and high temperature PEMFC, Int. J. Hydrogen Energy 44 (38) (2019) 21080–21089.
[7] Y. Gao, M. Lin, Research on the performance characteristics of hydrogen circulation pumps for PEMFC vehicles, Int. J. Hydrogen Energy (2023).
[8] O.B. Rizvandi, S. Yesilyurt, A transient Pseudo-3D model of the PEM fuel cell for the analysis of dead-ended anode and anode bleeding operation modes, Electrochim. Acta 324 (2019) 134866.
[9] C. Zhang, Z. Liu, W. Zhou, et al., Dynamic performance of a high-temperature PEM fuel cell–An experimental study, Energy 90 (2015) 1949–1955.
[10] F. Migliardini, T.M. Di Palma, M.F. Gaele, et al., Hydrogen purge and reactant feeding strategies in self-humidified PEM fuel cell systems, Int. J. Hydrogen Energy 42 (3) (2017) 1758–1765.
[11] X. Wang, Y. Lu, B. Zhang, et al., Experimental analysis of an ejector for anode recirculation in a 10 kW polymer electrolyte membrane fuel cell system, Int. J. Hydrogen Energy 47 (3) (2022) 1925–1939.
[12] Q. Jian, L. Luo, B. Huang, et al., Experimental study on the purge process of a proton exchange membrane fuel cell stack with a dead-end anode, Appl. Therm. Eng. 142 (2018) 203–214.
[13] K. Nikiforow, H. Karimäki, T.M. Keränen, et al., Optimization study of purge cycle in proton exchange membrane fuel cell system, J. Power Sources 238 (2013) 336–344.
[14] B. Wang, H. Deng, K. Jiao, Purge strategy optimization of proton exchange membrane fuel cell with anode recirculation, Appl. Energy 225 (2018) 1–13.
[15] S.W. Tsai, Y.S. Chen, A mathematical model to study the energy efficiency of a proton exchange membrane fuel cell with a dead-ended anode, Appl. Energy 188 (2017) 151–159.
[16] B. Chen, J. Wang, T. Yang, et al., Carbon corrosion and performance degradation mechanism in a proton exchange membrane fuel cell with dead-ended anode and cathode, Energy 106 (2016) 54–62.

[17] Z. Liu, J. Chen, H. Liu, et al., Anode purge management for hydrogen utilization and stack durability improvement of PEM fuel cell systems, Appl. Energy 275 (2020) 115110.

[18] J.J. Hwang, Effect of hydrogen delivery schemes on fuel cell efficiency, J. Power Sources 239 (2013) 54–63.

[19] Y. Liu, B. Xiao, J. Zhao, et al., Performance degradation of a proton exchange membrane fuel cell with dual ejector-based recirculation, Energy Convers. Manag. X 12 (2021) 100114.

[20] J. Liang, B. Wang, Y. Yin, et al., Experimental investigation of operating characteristics of proton exchange membrane fuel cell with different anode strategies based on the segmented cell, Int. J. Green Energy 21 (4) (2024) 798–815.

[21] Y. Liu, Z. Tu, S.H. Chan, Water management and performance enhancement in a proton exchange membrane fuel cell system using optimized gas recirculation devices, Energy 279 (2023) 128029.

[22] S. Toghyani, E. Afshari, E. Baniasadi, A parametric comparison of three fuel recirculation system in the closed loop fuel supply system of PEM fuel cell, Int. J. Hydrogen Energy 44 (14) (2019) 7518–7530.

[23] X. Kong, J. Han, Y. Guo, et al., Investigation on the pressure fluctuation of hydrogen Roots pump with a novel reflow structure for fuel cell vehicles, Int. J. Hydrogen Energy 50 (2024) 66–78.

[24] J. Feng, L. Xing, B. Wang, et al., Effects of working fluids on the performance of a roots pump for hydrogen recirculation in a PEM fuel cell system, Appl. Sci. 10 (22) (2020) 8069.

[25] L. Xing, J. Feng, W. Chen, et al., Development and testing of a roots pump for hydrogen recirculation in fuel cell system, Appl. Sci. 10 (22) (2020) 8091.

[26] X. Liang, H. Kang, J. Shen, et al., Review and analysis of hydrogen recirculation devices for compact vehicular proton exchange membrane fuel cells, J. Power Sources 555 (2023) 232308.

[27] J. Han, J. Feng, P. Chen, et al., A review of key components of hydrogen recirculation subsystem for fuel cell vehicles, Energy Convers. Manag. X 15 (2022) 100265.

[28] D.T. Le Tri, H.N. Vu, J. Woo, et al., Optimization of the ejector parameters for anodic recirculation systems in high-performance dual-stack proton-exchange membrane fuel cells, Energy Convers. Manag. 296 (2023) 117712.

[29] A. Khalilnejad, G.H. Riahy, A hybrid wind-PV system performance investigation for the purpose of maximum hydrogen production and storage using advanced alkaline electrolyzer, Energy Convers. Manag. 80 (2014) 398–406.

[30] B. Sezgin, Y. Devrim, T. Ozturk, et al., Hydrogen energy systems for underwater applications, Int. J. Hydrogen Energy 47 (45) (2022) 19780–19796.

[31] D.T. Le Tri, H.N. Vu, H.L. Nguyen, et al., A comparative study of single and dual ejector concepts for anodic recirculation system in high-performance vehicular proton exchange membrane fuel cells, Int. J. Hydrogen Energy 48 (70) (2023) 27344–27360.

[32] P. Pei, P. Ren, Y. Li, et al., Numerical studies on wide-operating-range ejector based on anodic pressure drop characteristics in proton exchange membrane fuel cell system, Appl. Energy 235 (2019) 729–738.

[33] J. Dong, Q. Hu, M. Yu, et al., Numerical investigation on the influence of mixing chamber length on steam ejector performance, Appl. Therm. Eng. 174 (2020) 115204.

[34] X. Wang, S. Xu, C. Xing, Numerical and experimental investigation on an ejector designed for an 80 kW polymer electrolyte membrane fuel cell stack, J. Power Sources 415 (2019) 25–32.

[35] J. Bian, Y. Zhang, Y. Liu, et al., Structural optimization of hydrogen recirculation ejector for proton exchange membrane fuel cells considering the boundary layer separation effect, J. Clean. Prod. 397 (2023) 136535.

[36] Z. Liu, Z. Liu, K. Jiao, et al., Numerical investigation of ejector transient characteristics for a 130-kW PEMFC system, Int. J. Energy Res. 44 (5) (2020) 3697–3710.

[37] Y. Yin, M. Fan, K. Jiao, et al., Numerical investigation of an ejector for anode recirculation in proton exchange membrane fuel cell system, Energy Convers. Manag. 126 (2016) 1106–1117.

[38] Y. Yang, W. Du, T. Ma, et al., Numerical studies on ejector structure optimization and performance prediction based on a novel pressure drop model for proton exchange membrane fuel cell anode, Int. J. Hydrogen Energy 45 (43) (2020) 23343–23352.

[39] Y. Song, L. Wang, L. Jia, et al., Optimization and performance investigation of confocal twin-nozzle ejector for PEMFC hydrogen supply and recirculation system under actual variable operating conditions, Int. J. Hydrogen Energy 50 (2024) 1450–1464.

[40] J. Han, G. Besagni, R. Mereu, et al., Performance investigation on the bypass ejector for a proton exchange membrane fuel cell system, Appl. Therm. Eng. 241 (2024) 122349.

[41] M. Yu, C. Wang, L. Wang, et al., Auxiliary-ejector-based hydrogen recirculation system to broaden PEMFC operating range, Int. J. Hydrogen Energy 57 (2024) 515–529.

[42] Y. Yang, X. Zhu, Y. Yan, et al., Performance of supersonic steam ejectors considering the nonequilibrium condensation phenomenon for efficient energy utilisation, Appl. Energy 242 (2019) 157–167.

[43] G. Zhang, X. Zhang, D. Wang, et al., Performance evaluation and operation optimization of the steam ejector based on modified model, Appl. Therm. Eng. 163 (2019) 114388.

[44] J. Han, J. Feng, X. Peng, Phase change characteristics and their effect on the performance of hydrogen recirculation ejectors for PEMFC systems, Int. J. Hydrogen Energy 47 (2) (2022) 1144–1156.

[45] Y. Li, C. Niu, S. Shen, et al., Double choking characteristics of three-dimensional steam ejector with non-equilibrium condensing, Appl. Therm. Eng. 211 (2022) 118446.

[46] H. Ding, Y. Dong, Y. Zhang, et al., Energy efficiency assessment of hydrogen recirculation ejectors for proton exchange membrane fuel cell (PEMFC) system, Appl. Energy 346 (2023) 121357.

[47] Y. Li, S. Shen, C. Niu, et al., The effect of variable motive pressures on the performance and shock waves in a supersonic steam ejector with non-equilibrium condensing, Int. J. Therm. Sci. 185 (2023) 108034.

[48] M. Yu, C. Wang, L. Wang, et al., Flow characteristics of coaxial-nozzle ejector for PEMFC hydrogen recirculation system, Appl. Therm. Eng. 236 (2024) 121541.

[49] J. Han, Y. Chen, J. Feng, et al., Condensation and droplet characteristics in hydrogen recirculation ejectors for PEM fuel cell systems, Int. J. Heat Mass Tran. 222 (2024) 125098.

[50] H. Ding, Y. Dong, Y. Zhang, et al., Exergy performance analysis of hydrogen recirculation ejectors exhibiting phase change behaviour in PEMFC applications, Energy 300 (2024) 131563.

[51] S. Wang, D. Jin, Y. Zhang, et al., A forward-curved blade centrifugal compressor for anode recirculation in proton exchange membrane fuel cells, Int. J. Hydrogen Energy 53 (2024) 736–748.

[52] D. Jenssen, O. Berger, U. Krewer, Improved PEM fuel cell system operation with cascaded stack and ejector-based recirculation, Appl. Energy 195 (2017) 324–333.

[53] X. Kong, J. Han, Y. Chen, et al., Performance investigation of coupling modes for hydrogen circulation in high-power proton exchange membrane fuel cell systems, Int. J. Hydrogen Energy 71 (2024) 1255–1265.

[54] D. Chong, J. Yan, G. Wu, et al., Structural optimization and experimental investigation of supersonic ejectors for boosting low pressure natural gas, Appl. Therm. Eng. 29 (14–15) (2009) 2799–2807.

[55] H. Ding, Y. Zhang, C. Sun, et al., Numerical simulation of supersonic condensation flows using Eulerian-Lagrangian and Eulerian wall film models, Energy 258 (2022) 124833.

[56] D. Hu, Y. Wang, J. Li, et al., Investigation of optimal operating temperature for the PEMFC and its tracking control for energy saving in vehicle applications, Energy Convers. Manag. 249 (2021) 114842.

[57] Y. Yu, M. Chen, S. Zaman, et al., Thermal management system for liquid-cooling PEMFC stack: from primary configuration to system control strategy, eTransportation(Amsterdam) 12 (2022) 100165.

[58] J. Zhao, S. Li, Z. Tu, Development of practical empirically and statistically-based equations for predicting the temperature characteristics of PEMFC applied in the CCHP system, Int. J. Hydrogen Energy 52 (2024) 894–904.

[59] H. Ding, Y. Zhao, C. Wen, et al., Energy efficiency and exergy destruction of supersonic steam ejector based on nonequilibrium condensation model, Appl. Therm. Eng. 189 (2021) 116704.

[60] F.R. Menter, Two-equation eddy-viscosity turbulence models for engineering applications, AIAA J. 32 (8) (1994) 1598–1605.

[61] J. Bodys, J. Smolka, M. Palacz, et al., Non-equilibrium approach for the simulation of CO2 expansion in two-phase ejector driven by subcritical motive pressure, Int. J. Refrig. 114 (2020) 32–46.

[62] A. Kantrowitz, Nucleation in very rapid vapor expansions, J. Chem. Phys. 19 (9) (1951) 1097–1100.

[63] F. Bakhtar, J.B. Young, A.J. White, et al., Classical nucleation theory and its application to condensing steam flow calculations, Proc. IME C J. Mech. Eng. Sci. 219 (12) (2005) 1315–1333.

[64] G. Zhang, S. Dykas, S. Yang, et al., Optimization of the primary nozzle based on a modified condensation model in a steam ejector, Appl. Therm. Eng. 171 (2020) 115090.

[65] J. Tan, D. Zhang, L. Lv, A review on enhanced mixing methods in supersonic mixing layer flows, Acta Astronaut. 152 (2018) 310–324.

[66] A. Fluent, 18.0 ANSYS Fluent Theory Guide 18.0, Ansys Inc., 2017.

[67] W.L. Oberkampf, T.G. Trucano, Verification and validation in computational fluid dynamics, Prog. Aero. Sci. 38 (3) (2002) 209–272.

[68] K. Nikiforow, P. Koski, H. Karimäki, et al., Designing a hydrogen gas ejector for 5 kW stationary PEMFC system–CFD-modeling and experimental validation, Int. J. Hydrogen Energy 41 (33) (2016) 14952–14970.